INTERNATIONAL JOURNAL OF AUTOMOTIVE SCIENCE AND TECHNOLOGY

2023, VOL. 7, NO: 3, 234-247 www.ijastech.org e-ISSN: 2587-0963

Modelling and Fault Diagnosis of Lithium-Ion Battery for Electric Powertrain

Adrien Soloy[1*], Thomas Bartoli[1], Fatima Haidar[1]

0000-0003-4582-6335, 0000-0002-9460-9639, 0000-0003-4805-844X

[1]*Capgemini Engineering, Research & Innovation Direction, 12 rue de la Verrerie, 92190, Meudon, France*

Abstract

The aim of this study is to create a lithium-ion battery pack model using a Matlab-Simulink interface. The model created consists of an equivalent circuit model, an ageing model and a fault mode. The equivalent circuit model allows to calculate the voltage and current evolution during cycling and the relaxation phase of the cells. The ageing model simulates the degradation behavior of the cells both from cycle and calendar ageing based on the Arrhenius equation. Contrary to existing models, our model can simulate the performances degradation in a short time scale in the order of seconds. Simulations were compared to experimental data and a good correlation was obtained for temperatures close to room temperature. The fault mode simulates a cell failure and its consequences regarding the current/voltage behavior of the battery pack. Unlike most of the existing modellings, this failure mode is not a predictive model, to predict when the failure will happen, but it gives a direct response for the regulation of the battery in case of a cell disconnection.

Keywords: Battery ageing; Battery pack faults; Cell relaxation time; Equivalent circuit; Lithium-ion battery modelling; Matlab-Simulink; State of charge; WLTC

Research Article

https://doi.org/10.30939/ijastech..1295130

Received 11.05.2023
Revised 28.06.2023
Accepted 07.07.2023

* Corresponding author
Adrien SOLOY
adrien.soloy@capgemini.com
Address: Capgemini Engineering, Research & Innovation Direction, 12 rue de la Verrerie, 92190, Meudon, France
Tel: +33658210653

1. Introduction

Environmental concerns about the depletion of conventional energy sources have increased worldwide over the past decades. One of the main causes of the increase of atmospheric pollution and greenhouse effect is the abundant use of fossil fuels, especially in automotive applications [1].

To reduce the environmental impact, automotive manufacturers in Europe focused on achieving the EU fleet-wide average emission standard of less than 95 g of CO2/km by 2021 with fuel consumption of around 4.1 l/100 km of petrol or 3.6 l/100 km of diesel. A further reduction of 15%, decreasing the emission standards down to 81 g of CO2/km will have to be achieved by 2025 and they will be set to 59 g of CO2/km in 2030 [2].

Many research projects have been launched in the field of hybrid electric (HEV) and electric vehicles (EV) to achieve this goal. These two types of vehicles can significantly reduce the exhaust emissions compared to conventional vehicles [3]. Besides, there are many ways of producing electricity. In France, nuclear power plants produce 75% of the electricity [4], which decreases the carbon footprint of an electric vehicle to less than 20 g of CO2/km from the tank to the wheel. Consequently, the deployment of EV has increased sharply over the past ten years. In 2018, the global stock of electric passenger cars has increased by 63% compared to the previous year and passed 5 million units.

In the development of HEV and EV, energy storage is a significant issue. A lot of effort in research was conducted to optimize the energy storage with improved cyclability and higher energy density [5–7]. Battery manufacturers are mainly interested in lithium-ion technologies which have high specific energy (Wh/kg), high specific power (W/kg) and promising low costs [8]. Based on the electrode and electrolyte materials, several types of lithium-ion batteries are available on the market. The most commonly used are C/LFP (LixC6/LiFePO4) and C/NMC (LixC6/Li[NixMnyCoz]O2) batteries [8,9].

In a simplified approach of a powertrain simulation, the battery pack is often considered as a constant voltage source. However, a lithium battery is a dynamic electrochemical system: the supplied voltage, the rated capacity, the internal impedance, and the power vary according to several conditions, including the State of Charge (SoC), the State of Health (SoH), the temperature and the current demand. A Battery Management System (BMS) model should be able to detect the individual information of every cell / sub-module in the pack when it is assembled into the battery pack model. As a result, the realistic modelling, which gathers detailed information from every battery cell, sub-module and the pack, becomes complex.

In this context, a cell-to-pack lithium-ion battery model was developed and is presented in the following sections. For each cell of

the battery pack, the model calculates the voltage and current evolution during cycling and relaxation phase through the equivalent circuit model. The ageing model simulates the individual degradation behavior from both cycle and calendar ageing based on the Arrhenius equation. In literature, ageing modellings are based on ageing experiments with steady conditions: the temperature, the solicitation current or the SoC is maintained at a given level. Moreover, the modelling is performed on very large time scales. For instance, the calendar ageing modellings of Redondo et al. [10] and of Badey et al. [11] are based on a time scale of several hundred days. The cycling ageing modellings of Jalkanen et al. [12] and Gao et al. [13] are based on a time scale of several hundreds and thousands of cycles. These modellings are accurate on a long duration, but they do not allow degradation simulations on a short time scale. Contrary to existing models, the model developed in our work is able to model the performances degradation in a short time scale in the order of seconds. As this battery pack model relies on individual cell modelling, it was ideal to also implement a fault mode, as part of the BMS model. In industry, the Weibull distribution is often used the predict the failure of a Li-ion battery over time [14,15]. However, in our work, the failure modelling will be focused on the consequences regarding the electrical parameters and not the causes, in order to develop a BMS with relevant control command laws in case of failure. Contrary to existing models, our model is not meant to predict when the failure will occur but rather to control the battery in case of a failure and predict the impact of a scheduled failure.

The aim of this study is to create a battery model containing an equivalent circuit model, cycle and calendar ageing models and a fault mode with the features previously described. This model will then be integrated into a simulation platform of a complete powertrain of a vehicle. This battery model will allow to implement a full electrical power supply system within the powertrain simulation platform, coupling the BMS and the battery model together. In the purpose of developing a thorough controlling strategy, the battery model will not only simulate the cell behavior but the battery pack behavior as well. The model will also simulate the failure of individual cells in order to develop a risk strategy management for the BMS. The work described here will not detail the integration of the battery model within the simulation platform but will rather focus on the method used to develop the battery model itself.

2. Model description and methodology

This section presents the main sub-models of the individual cell model, the equivalent circuit model, and the ageing model. As expressed in the previous section, the model is developed under industrial simulation needs. Therefore, efficient but straightforward modelling methods were used to limit the computational costs while maintaining a good accuracy.

2.1 Equivalent Circuit Model

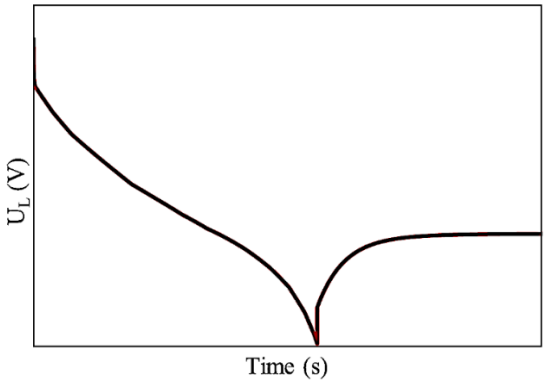

Fig. 1. Discharge and relaxation phase of a lithium-ion battery.

Li-ion battery cell voltage, on which relies most of battery management strategies, is influenced by several parameters such as the SoC, the current load, and the temperature. Because of its electrochemical nature, a lithium-ion cell exhibits noticeable transient modes under dynamic loads. When the current load stops, the voltage keeps evolving until reaching the Open-Circuit Voltage (OCV). This transient mode is called the relaxation phase, its time range is relatively long compared to the transient phase when the cell is solicited (usually a few hours). The Figure 1 shows a general voltage evolution of a lithium-ion battery during a discharge and a relaxation phase. In order to simulate the electrical behavior and the voltage evolution of lithium-ion batteries, several types of equivalent circuit models were published in the literature, such as the Rint model, the Thevenin model and the Dual Polarization (DP) model [16–18]. Among all these models, the DP model, shown in Figure 2, was chosen for the equivalent circuit modelling. This model gives not only excellent electrical performance but also a good chemical interpretation for the lithium-ion battery behavior. The internal series resistance represents the electronic conductivity. The first $R_{pa}C_{pa}$ circuit simulates the charge transfer effect and the $R_{pc}C_{pc}$ circuit simulates the mass transfer effect. By applying the DP model, the voltage behavior under cycling and the voltage evolution during the relaxation phase were determined.

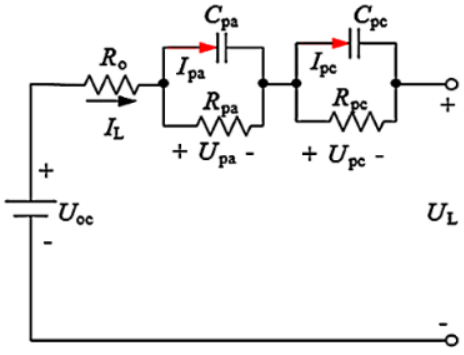

Fig. 2. DP equivalent circuit model [17].

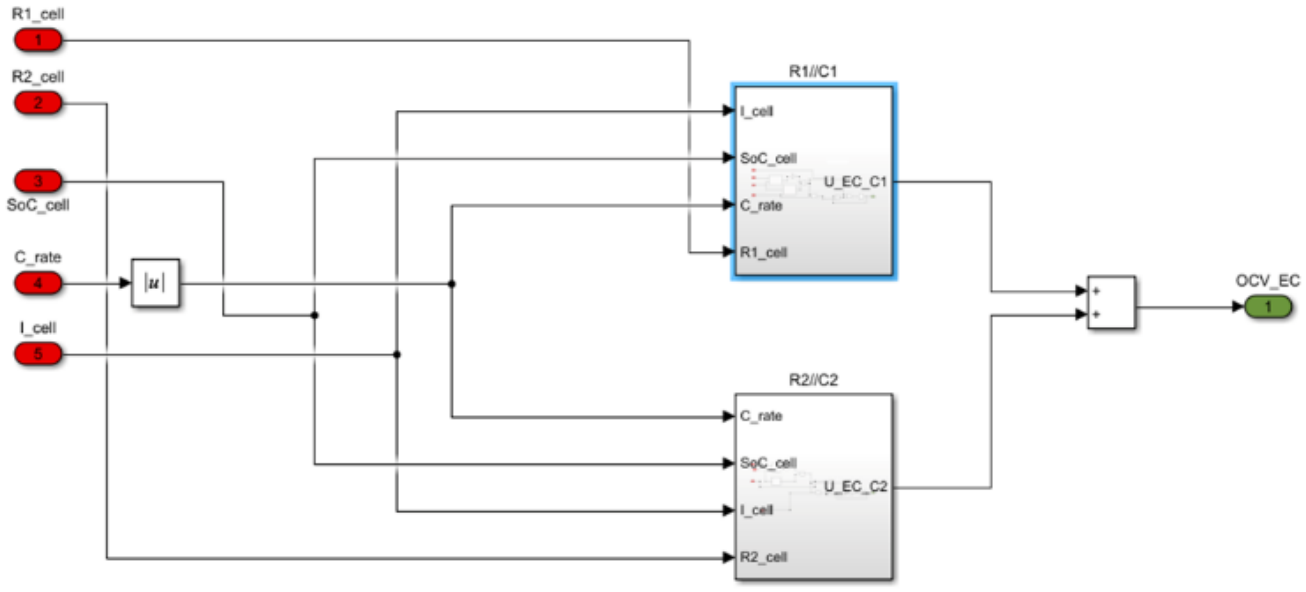

Fig. 3. Simulink model of the equivalent circuit

The electrical behavior of the circuit is calculated using the following equations Eq. (1) :

$$\begin{cases} dU_{pa}/dt = \frac{U_{pa}}{R_{pa}C_{pa}} - \frac{I_L}{C_{pa}} \\ dU_{pc}/dt = \frac{U_{pc}}{R_{pc}C_{pc}} - \frac{I_L}{C_{pc}} \\ U_L = U_{OC} + U_{pa} + U_{pc} + I_L R_0 \end{cases} \quad (1)$$

U_{pa} and U_{pc} are the voltages, I_{pa} and I_{pc} are the outflow currents and U_{OC} is the open-circuit voltage which is implemented by a Look-up table function in Simulink.

By analyzing the existing data published by Madani et al. [18], it was noticed that the value of the two capacitances and the value of the three resistances are not always constant under different conditions. The values of C_{pa} and C_{pc} are strongly influenced by the applied current and the SoC level. On the other hand, the applied current has almost no effect on the three resistance values. Compared to the value of R_{pa}, the values of R_0 and R_{pc} are less dependent on the SoC level [17]. Therefore, a dynamic parameter calculation system was applied to make the equivalent circuit model more accurate. The identification of specific parameter values and their variations are detailed in the results.

The Figure 3 shows the implementation of the equivalent circuit model with 2 different blocks for the 2 RC parallel circuits.

2.2 Relaxation model

Stimulated ions return to an equilibrium state during the relaxation phase, which is relatively slow. The existing relaxation models usually use a succession of parallel RC circuits [17]. The number of circuits depends on the voltage variation during the relaxation phase. To simulate the relaxation behaviors, this phase was divided into several parts. Each part is represented by a RC circuit.

In this case, the equivalent circuit model already contains two RC circuits and a resistance in series. Therefore, to reduce computational cost, the relaxation phase was modeled by using the DP model already implemented and changing the value of the two capacitances.

From the electronic engineering's point of view, the equivalent circuit model is a Linear Time-Invariant (LTI) system, where the voltage U_L behavior is described as an exponential decay and indicated by the time constant τ. When the battery cell is cycled, the current charges the capacitances C_{pa} and C_{pc}. Once the current is removed, the capacitances C_{pa} and C_{pc} are discharged which bring the cell voltage to the corresponding OCV value at the end of the relaxation phase. The relaxation time t_{rel} is considered to be 5τ such as:

$$\boldsymbol{t_{rel} = 5\tau = 5R_{pa}C_{pa} = 5R_{pc}C_{pc}} \quad (2)$$

At this point, the voltage discharged by each RC circuit is proportional to the corresponding resistance. As shown in literature [19], R_{pa} (stable phase) takes 35% of the total resistance, R_{pc} takes 15% of the total resistance, and R_0 takes 50% of the total resistance. So, during the relaxation, the $R_{pa}C_{pa}$ circuit, the $R_{pc}C_{pc}$ circuit and the series resistance R_0 take respectively 35%, 15% and 50% of the voltage variation.

2.3 Battery pack model

When assembled with other components of the powertrain, the battery pack model handles a current request and provides a resultant voltage value, leading to the supplied power. To simulate the battery pack's response, the information of each cell must be summarized, and the input current distributed to each cell by applying the Kirchhoff laws. In the Kirchhoff laws, an electrical circuit is considered as a combination of meshes and nodes. For each node, the sum of the incoming currents is equal to the sum of the outgoing currents (Eq. (3)). For each mesh, the sum of the voltage along the border is equal to zero (Eq. (4)).

$$\sum_1^j I_{ij} = 0 \quad (3)$$

$$\sum_1^j (OCV_{1j} + I_{1j}R_{1j}) = \sum_1^j (OCV_{2j} + I_{2j}R_{2j}) = \cdots$$
$$= \sum_1^j (OCV_{ij} + I_{ij}R_{ij}) \quad (4)$$

In this work, the typical commercialized battery structure, which includes a significant number of cells arranged in series and parallel, was reproduced. Solving the Kirchhoff laws in such structure causes the computational process to be very complicated. Therefore, two matrices were used to implement the Kirchhoff laws in Matlab. One represents all the nodes, and the other one represents all the meshes. Those two matrices represent the way the cells are connected within the battery pack. The two matrices are shown in Figure 4.

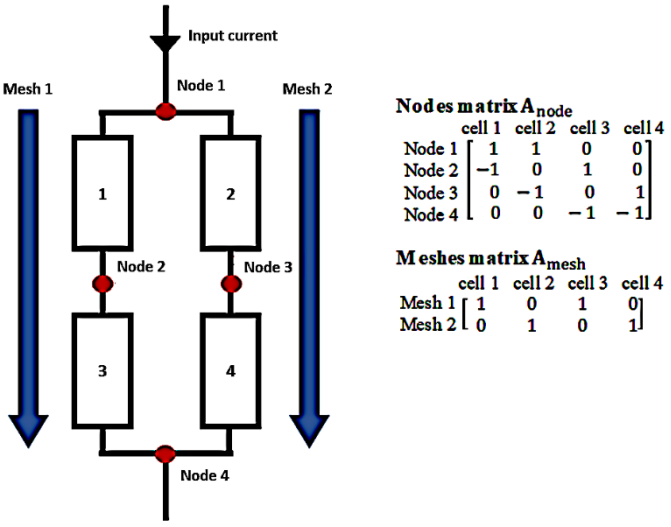

Fig. 4. System defined by the matrices of the nodes and meshes.

In the nodes matrix, each line represents a node, and each column represents a cell. The value of each element in the matrix depends on the connection of the cell to the given node. If the cell is not connected to the node, the element value is equal to zero. If the cell is connected to the node through the inlet of current, the element value is equal to 1. Otherwise, it is equal to -1.

Regarding the meshes matrix, each line represents a mesh, and each column represents a cell. In this matrix, the element value is equal to 1 when a cell is on the mesh. In the opposite, the element value is equal to zero. Besides these two matrices, each cell's resistance R_{s_real} is gathered into another matrix B_{res}.

Solving the Kirchhoff laws, thanks to the Equations 3 and 4, allows to determine the current and voltage across each cell, allowing in the end to ensure the distribution of the current and the determination of the total voltage of the battery pack.

By redistributing the pack current into cells currents, the model then calculates the thermal effect, the cell's SoC and the ageing effect. The logic flow of the entire battery model is presented in Figure 5.

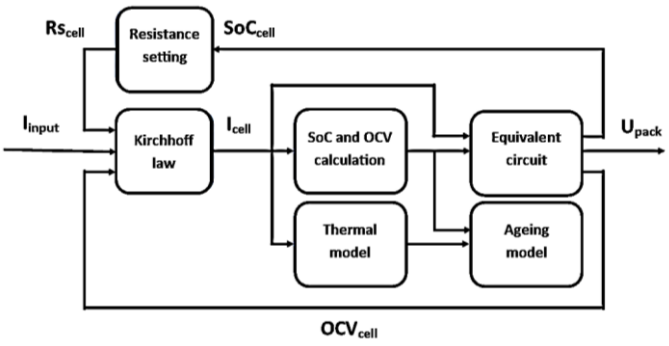

Fig. 5. Logic flow of the battery model.

2.4 Cell failure model

According to studies, there can be a large variety of causes of Li-ion battery failure [20]. Deep discharges may cause lithium plating on the surface of the negative electrode during recharging. If the battery is charged with a strong current, Li dendrites may grow, go through the separator, and cause a short-circuit. When charging up to high potentials, heating can occur, enhancing parasitic degradation reactions of the electrolyte. Those degradation reactions may lead to an even larger heating, causing a thermal runaway. If the battery is stored in non-ideal conditions, the calendar ageing of the battery will be affected, enhancing the capacity loss and increasing the internal resistance. During a mechanical shock, there is a risk of separators breaking, causing an internal short-circuit of the lithium-ion battery. When the charging station is damaged (bad connection), a cell can be disconnected from the circuit, disturbing the performance of the complete battery pack.

In industry, the Weibull distribution is often applied to predict the failure of various components as a function of time [14,15,20]. In our case, it was intended to simulate the consequences of a battery failure more so than the causes, in order to allow the development of an efficient BMS and the design of an appropriate command and control algorithm to manage the failure.

Therefore, the consequences of a failure, appearing at a specific time designated by users, were implemented. Two consequences of failure were studied: the disconnection and the short circuit of a cell. The failure simulation is performed by modifying the internal resistance value abruptly during the simulation.

When a specific cell is chosen to be disconnected at a given time, its internal resistance increases to 20 kΩ. Using this simulation strategy and with a constant current draw of 28 A, the results shown in Figure 6 were obtained. The simulation is done on a 4-cell system with two different configurations. The system on the left (Figure 6a) is in a series/parallel connection configuration. The system on the right (Figure 6b) is in a parallel/series configuration. The cell n°1 is set to be disconnected from the circuit after 1000 s.

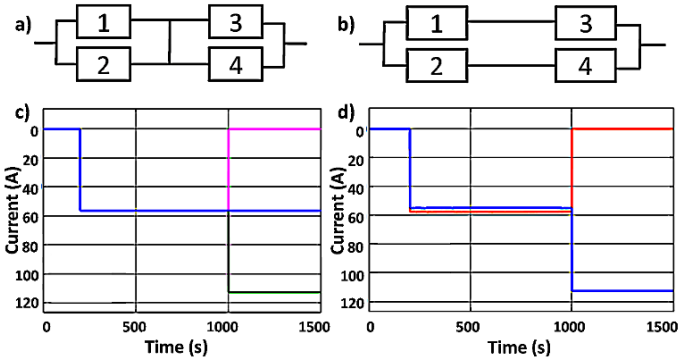

Fig. 6. Four cell system in series/parallel (a) and in parallel/series configuration (b) and their corresponding cell failure simulation results (c, d) with the current going through cell n°1 (pink), cell n°2 (green), cell n°3 (orange) and cell n°4 (blue).

Figure 6c and Figure 6d show a 1C discharge curve and the relaxation phase after discharge for the series/parallel and the parallel/series configuration respectively. The results show that for a series/parallel configuration, when cell n°1 is disconnected from the circuit, its current becomes 0, as expected. The total current flows through cell n°2. The sub-circuit made of cell n°3 and cell n°4 is not affected. For the parallel/series configuration, when cell n°1 is disconnected from the circuit, the complete branch made of cell n°1 and cell n°3 is cut-off and the current drops to zero immediately. Consequently, the branch of cell n°2 and cell n°4 supports the total current. These behaviors are consistent with the real case scenarios. It is noticed that when the parallel RC circuits are not integrated into the model, the voltage drop is instantaneous as well as the voltage recovery after stress.

2.5 Ageing model

In the previous section, the cell models for electrical behavior were presented. In this section, the chemical behavior of a lithium-ion battery cell regarding ageing is discussed. The reasons for battery ageing, such as lithium deposition and the formation of Solid Electrolyte Interphase (SEI), are widely studied in the literature [21].

The ageing phenomenon is expressed in two degradation forms, the loss of capacity and the increase of resistance. To simulate these two consequences, an ageing model based on classical empirical models, was developed. These models focus on simulating the ageing effects with constant conditions (SoC, temperature, current) in the long run [10,12,13,22]. These models are usually accurate over a long period of time at steady conditions. Unlike most of existing ageing models that cannot simulate degradation neither over a short period of time (a few seconds), nor in evolutive conditions, the objective of this ageing model is to simulate the instantaneous degradation of a lithium-ion battery, since the current and the temperature are not constant when the battery pack supplies energy to the powertrain.

The ageing model is divided into two components, the cycle ageing and calendar ageing, represented by two different equation packages. The ageing model switches from one ageing mode to another depending on if the vehicle is being driven or parked.

2.5.1 Calendar ageing

According to E. Redondo et al. [10], calendar ageing is a temperature-sensitive chemistry process that can be described by the Arrhenius law. The usual equations Eq. (5) and Eq. (6) were put into their integral form to determine the instantaneous ageing [10]. To switch from a time scale in days to a time scale in seconds, in order to calculate the degradation effects in periods of time in the order of seconds, the equations Eq. (5) and Eq. (6) were modified into Eq. (7) and Eq. (8) respectively as follows:

$$Q_{loss}^{cal} = A_c \cdot e^{\left(-\frac{Ea_c}{K \cdot T}\right)} \cdot t^Z \quad (5)$$

$$R_{rise}^{cal} = A_r \cdot e^{\left(-\frac{Ea_r}{K \cdot T}\right)} \cdot t^Z \quad (6)$$

$$Q_{loss}^{cal} = \sqrt{\int_0^D \frac{1}{86400} \cdot {A_c}^2 \cdot e^{\left(-\frac{2 \cdot Ea_c}{K \cdot T}\right)} dt} \quad (7)$$

$$R_{rise}^{cal} = \sqrt{\int_0^D \frac{1}{86400} \cdot {A_r}^2 \cdot e^{\left(-\frac{2 \cdot Ea_r}{K \cdot T}\right)} dt} \quad (8)$$

Q_{loss}^{cal} is the capacity loss and R_{rise}^{cal} is the resistance increase due to calendar ageing. A_c and A_r are the pre-exponential factors of the capacity loss and of the resistance increase due to calendar ageing respectively. Ea_c and Ea_r are the activation energies of the capacity loss and of the resistance increase due to calendar ageing respectively. K is the Boltzmann constant and T is the temperature. D is the test duration in seconds, t the time and z the power factor varying between 0.5 and 1. In the model, z is set to 0.5.

With the tests performed by Keil et al. [23], calendar ageing data of three different types of Li-ion battery cells (18650 LFP, NMC and NCA cells) were obtained for a duration of 300 days. For each type of battery, the tests were performed on identical cells coming from the same production batch under different conditions, at 3 different temperatures (25°C, 40°C and 50°C) and 16 different SoC levels, leading to 48 different calendar ageing conditions tested for each technology.

For every SoC level, the capacity loss and the resistance increase were obtained for the 3 different temperatures. A three linear equations system was then obtained and solved using the least squares method to determine values for A and Ea.

The results are presented in Figure 7. The evolution of the activation energies for the capacity loss and the resistance increase, Ea_c and Ea_r, are shown in Figure 7a and Figure 7c respectively.

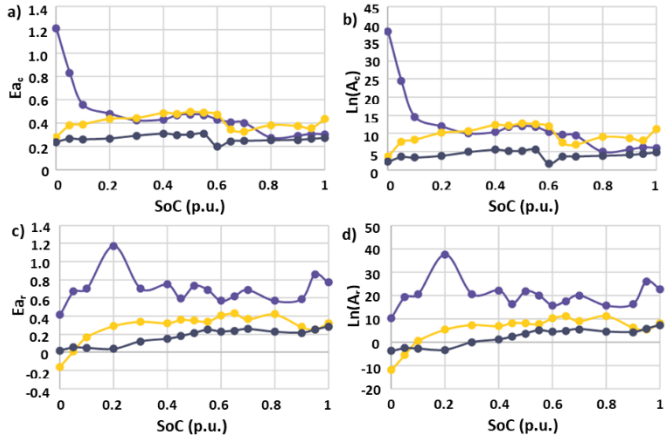

Fig. 7. Activation energies for capacity loss Eac (a) and for resistance increase Ear (c); and pre-exponential factors for capacity loss Ac (b) and for resistance increase Ar (d) as a function of the cell chemistry (LFP (purple), NMC (yellow) and NCA (black)) and the SoC. The SoC is expressed in p.u. (100%=1 p.u.)

The values for the pre-exponential factors for the capacity loss and the resistance increase, A_c and A_r, are presented in Figure 7b and Figure 7d respectively. The evolutions are shown as a function of the cell chemistry and the SoC. The data are expressed in per unit (p.u.) (100% = 1 p.u.).

The pre-exponential factors A_c and A_r and the activation energies Ea_c and Ea_r vary as a function of the SoC and cannot be simply expressed by mathematical equations. Therefore, the values were implemented by using Look-up tables in Simulink to calibrate the model for the three different technologies.

The validation of the chosen parameters is performed thanks to data from the article of Keil et al. [23]. The Figure 8 shows the data extracted from the article (the marks) and the results simulated with the calibrated model (the lines). A small standard deviation σ is obtained between the experimental and the simulated data. The Simulink model of the calendar ageing is represented in Figure 9. The inputs are the SoC and the temperature of each cell. The outputs are the resistance increase in Ω and the capacity loss in Ah. A switch function is used to deactivate the calendar ageing when the current is different from zero. Indeed, in that case, the cycle ageing is considered, and the calendar ageing effect is taken into account within the cycle ageing. So, the calendar ageing must not be considered when a current is applied to the cell.

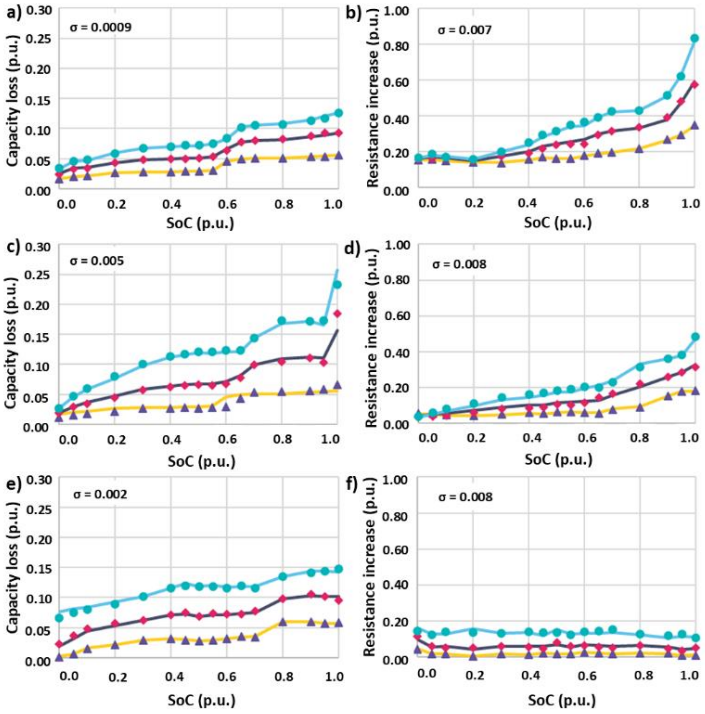

Fig. 8. Capacity loss (a, c, e) and resistance increase (b, d, f) obtained from the experimental data of Keil et al. [23] compared to the simulated data from the calendar ageing model. Tests performed for NCA cells after 300 days (a, b), NMC cells after 300 days (c, d) and LFP cells after 270 days (e, f) of calendar ageing respectively. Tests performed at 25°C (purple triangles), 40°C (red diamonds) and 60°C (blue circles) and simulated data obtained at 25°C (yellow line), 40°C (black line) and 60°C (blue line). The standard deviations (σ) between the experimental and the simulated data are given in each case. The data are expressed in p.u. (100%=1 p.u.).

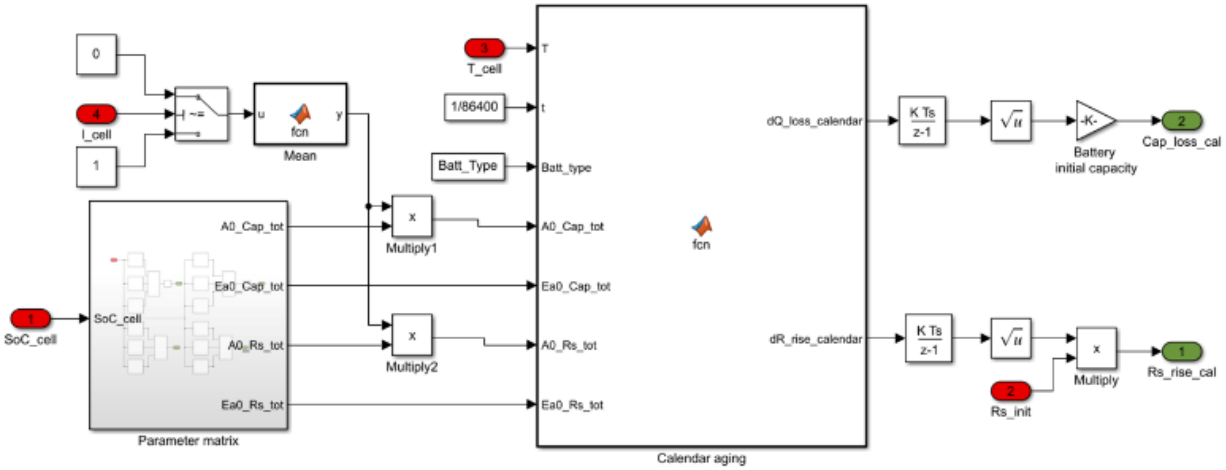

Fig. 9. Simulink model of the calendar ageing

2.5.2 Cycle ageing

In the literature, cycle ageing is often described as a function of the number of cycles [12,24]. In this case, the simulation time also needs to be expressed in function of time.

It was assumed that a cycle of cyclic ageing contains a complete discharge and a complete charge and that the difference between the charge and the discharge was neglectable. So, it was considered that the same amount of positive and negative current (stress) has the same influence on the chemical degradation of the battery.

Therefore, the ageing behavior of one cycle can be distributed over each instant. It is considered that for each cycle, the real-time is equal to 2 times the real capacity C_{real} divided by the current I (once during charge, once during discharge), as shown in the Eq. (9):

$$ds = 2 \cdot \frac{C_{real}}{I} \cdot 3600 dt \quad (9)$$

Then, to change from a number of cycles to a time in seconds, the following variable change must be carried out:

$$t = \int_0^{S_{fini}} \frac{I}{7200 \cdot C_{real}} ds \quad (10)$$

For the cycle ageing, the rate of capacity loss and resistance increase is influenced not only by the temperature but also by the current level. Therefore, the rate of charge and discharge C-rate has been added into the calculation. The loss of capacity and the increase of resistance are calculated through the Eq. (11) and Eq. (12) as followed:

$$Q_{loss}^{cyc} = 2A_c \cdot e^{\left(\frac{-Ea_c + B_c \cdot C_{rate}}{R \cdot T}\right)} \cdot t^z \quad (11)$$

$$R_{rise}^{cyc} = A_r \cdot e^{\left(\frac{-Ea_r + B_r \cdot C_{rate}}{R \cdot T}\right)} \cdot t^z \quad (12)$$

Q_{loss}^{cyc} is the capacity loss and R_{rise}^{cyc} is the resistance increase due to cycle ageing. A_c and A_r are the pre-exponential factors of the capacity loss and of the resistance increase for the cycle ageing respectively. Ea_c and Ea_r are the activation energies of the capacity loss and of the resistance increase due to cycle ageing respectively. C_{rate} is the cycling rate. B_c and B_r are the current accelerating factors, that adjust the impact of the C-rate, of the capacity loss and the resistance increase respectively. R is the perfect gas constant; t is the number of cycles and z is a power factor varying between 0.5 and 1. From the data given in the references [12] and [13], it was observed that cycle ageing behaviors evolved linearly with the number of cycles, so z was set to 1. After applying the variable change described in Eq. (10), the capacity loss and the resistance increase are then expressed under their integral form as followed in Eq. (13) and Eq. (14):

$$Q_{loss}^{cyc} = \int_0^{S_{fini}} A_c \cdot e^{\cdot\left(\frac{-Ea_c + B_c \cdot C_{rate}}{R \cdot T}\right)} \cdot \frac{I}{3600 C_{real}} \cdot ds \quad (13)$$

$$R_{rise}^{cyc} = \int_0^{S_{fini}} A_r \cdot e^{\cdot\left(\frac{-Ea_r + B_r \cdot C_{rate}}{R \cdot T}\right)} \cdot \frac{I}{3600 C_{real}} \cdot ds \quad (14)$$

S_{fini} is the cycle duration.

The parameters identification was carried out based on the data published by Yuksel et al. [25]. They identified the activation energy Ea_c and the acceleration factor A_c for a simpler cycle ageing model which doesn't consider the regime impact. They found that $A_c = A_r = 11443$ and $Ea_c = Ea_r = 42570$ J.mol^{-1}. Those values were reused as predefined parameters in this model. Regarding the values of B_c and B_r, they were calibrated from the data published by Gao et al. [13] using the least squares method. They investigated the cycle ageing behaviour of a LCO cell at different cycling rates (0.5C, 0.8C, 1C, 1.2C 1.5C) at a given temperature of 25°C. From the Eq. (11) and Eq. (12), it is observed that when the regime and the temperatures are fixed, the capacity loss and the resistance increase are linear as a function of time (or number of cycles). The data from Gao et al. [13] allow us to determine the values of K_c and K_r, which are the slopes of the evolution of capacity and resistance respectively. They are defined as follows:

$$K_c = 2A_c \cdot e^{\left(\frac{-Ea_c + B_c \cdot C_{rate}}{R \cdot T}\right)} \quad (15)$$

$$K_r = A_r \cdot e^{\left(\frac{-Ea_r + B_r \cdot C_{rate}}{R \cdot T}\right)} \quad (16)$$

The evolution of K_c and K_r as a function of C-rate is given in Figure 10. The evolution of K_c is not linear on the whole range of C-rate. However, K_c can be approximated with 2 linear functions with a R^2 larger than 0.95, on 2 different domains: C-rate lower or equal to 1 and C-rate larger than 1. Those 2 linear functions are described in Eq. (17) and Eq. (18) respectively. Their corresponding correlation factor R^2 are shown in Figure 10a. K_r is approximated by one linear function over the whole range of C-rate. This linear function is described in Eq. (19). Its corresponding correlation factor R^2 is shown in Figure 10b.

$$Kc_{C_{rate}>1} = 2.61 C_{rate} - 12.69 \quad (17)$$

$$Kc_{C_{rate}\leq 1} = 0.61 C_{rate} - 10.63 \quad (18)$$

$$K_r = 0.57 C_{rate} - 7.09 \quad (19)$$

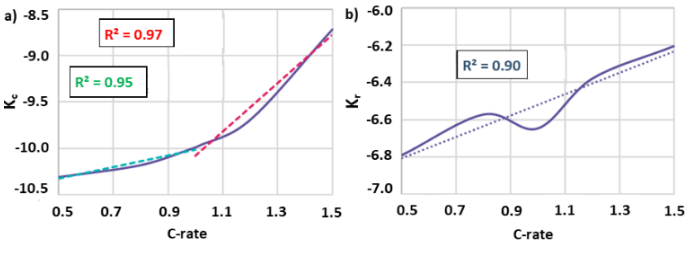

Fig. 10. Evolution of Kc (a) and Kr (b) as a function of C-rate and trend lines.

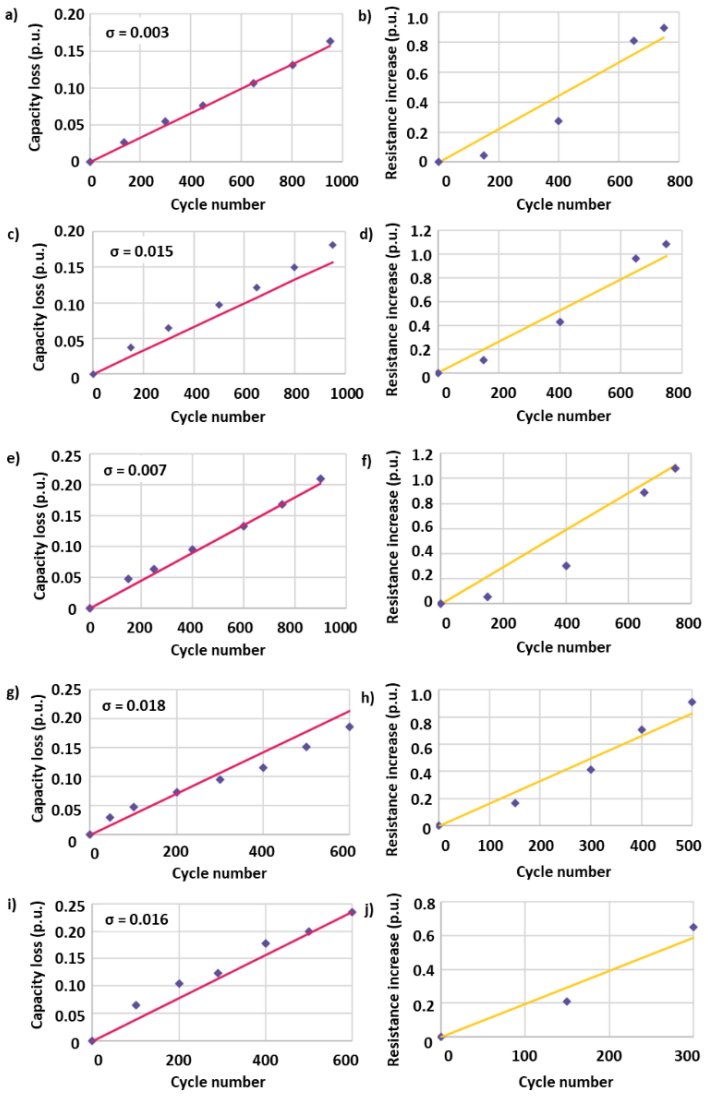

Fig. 11. Comparison between the simulated data (lines) obtained from the model and the experimental data (dots) from reference [13]. Capacity loss (a, c, e, g, i) and resistance increase (b, d, f, h, j) of LCO cells due to cycle ageing at a C-rate of 0.5C (a, b), 0.8C (c, d), 1C (e, f), 1.2C (g, h), 1.5C (i, j) at 25°C. The capacity losses and resistance increases are expressed in p.u. (100%=1 p.u.).

The values of B_c can then be determined for both C-rate ranges. For a C-rate lower or equal to 1, B_c is equal to 1515 and for a C-rate larger than 1, B_c is equal to 6480. The B_r value is determined on the whole C-rate range, it is equal to 1418. The value of Ea_c and Ea_r were determined accordingly. Ea_c is equal to 49513 when the C-rate is lower or equal to 1, Ea_c is equal to 54625 when the C-rate is larger than 1 and Ea_r is equal to 40742. The model was calibrated thanks to those values.

After the calibration of the model, simulated data were obtained and compared to the experimental data obtained from the tests presented in the work of Gao et al. [13]. The comparison between the simulated and the experimental data is presented in Figure 11. In their work, Gao et al. studied the capacity loss and resistance increase of LCO cells at different cycling rates (0.5C, 0.8C, 1C, 1.2C 1.5C) and at a given temperature of 25°C. Good correlation is obtained between the simulated (lines) and the experimental data (dots) regardless of the cycling rate.

The Simulink model of the cycle ageing is shown in Figure 12. The inputs are the current, the capacity, the initial series resistance, and the temperature. The outputs are the capacity loss and the resistance increase by cycle ageing. The absolute value of the current is used as it is considered that the charge and the discharge have the same effect on the performance degradation.

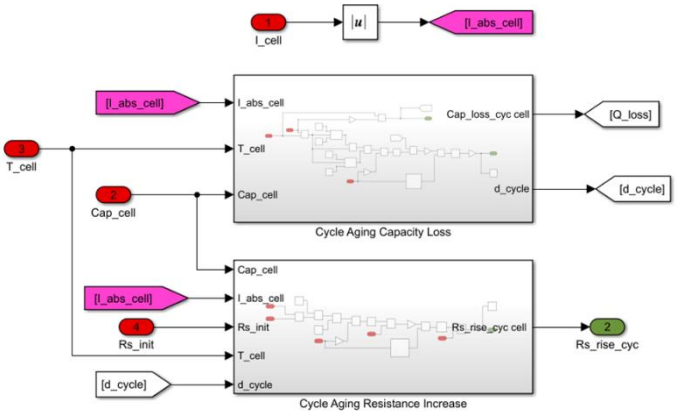

Fig. 12. Simulink model of the cycle ageing

3. Results and discussion

3.1 Equivalent circuit results

From the equation system Eq. (1), the following equation Eq. (20) can be deduced.

$$U_L = U_{OCV} + \int\left(\frac{U_{pa}}{R_{pa}C_{pa}} - \frac{I_L}{C_{pa}}\right) + \int\left(\frac{U_{pc}}{R_{pc}C_{pc}} - \frac{I_L}{C_{pc}}\right) + I_L R_0 \qquad (20)$$

The integration of this formula in Matlab-Simulink can be carried out using an integrator block but the simulations are time-consuming. Therefore, the quadrature rules were applied to the equivalent circuit model and the output potential was solved through the numerical integration form, as shown in the Eq. (21). Δt is the time step in seconds between the moment k and the moment k+1.

$$U_L = U_{OC} + U_{pa_k} + \frac{\Delta t \cdot U_{pa_k}}{R_{pa}C_{pa}} - \frac{\Delta t \cdot I_L}{C_{pa}} + U_{pc_k} + \frac{\Delta t \cdot U_{pc_k}}{R_{pc}C_{pc}} - \frac{\Delta t \cdot I_L}{C_{pc}} + I_L R_0 \qquad (21)$$

In order to maintain the accuracy of the equivalent circuit model, the time step Δt is equal to the time step of the model's input signal.

Concerning the applied parameters values, the data was analyzed based on the work of Madani et al. [18]. In their work, the same equivalent circuit was used. The experiments were performed on 5 different C-rates and 19 states of charge on a 13 Ah lithium titanate cell. They pointed out that the two capacitances

(C_{pa} and C_{pc}) and the three resistances (R_0, R_{pa} and R_{pc}) vary in function of the SoC and the current intensity of the cell.

By analyzing their data, two polynomial laws were established to approximate the variation of both capacitances, expressed through Eq. (22) and Eq. (23) as followed:

$$C_{pa} = A_{pa} \cdot (SoC)^2 + B_{pa} \cdot SoC + D_{pa} \quad (22)$$

$$C_{pc} = A_{pc} \cdot (SoC)^2 + B_{pc} \cdot SoC + D_{pc} \quad (23)$$

The parameters A_{pa}, B_{pa}, D_{pa}, A_{pc}, B_{pc} and D_{pc} can be expressed through polynomial functions of C-rate. The parameters of the polynomial functions were determined by using the least square method. The polynomial functions of C-rate were then established as followed:

$$A_{pa} = 58.57C_{rate}^2 - 745.13C_{rate} - 2000.3 \quad (24)$$

$$B_{pa} = -82.8C_{rate}^2 + 1191.3C_{rate} + 2714.7 \quad (25)$$

$$D_{pa} = -10.54C_{rate}^2 - 31.3C_{rate} + 308.85 \quad (26)$$

$$A_{pc} = 1075.1C_{rate}^2 - 5765.3C_{rate} - 1116.2 \quad (27)$$

$$B_{pc} = -1242.1C_{rate}^2 + 7555.4C_{rate} + 1013 \quad (28)$$

$$D_{pc} = 122.71C_{rate}^2 - 839.19C_{rate} + 1632 \quad (29)$$

As shown in Figure 13, good correlation is obtained between the evolution of those parameters and the polynomial functions of C-rate established to describe it. By using all these formulas, the capacitances can be estimated for different states of charge and C-rates. The approximated capacitance values are shown in Figure 14. The simulated capacitances are good approximations of the experimental data, especially for more important C-rates (2C and 4C). Furthermore, these parameters are extracted from a 13 Ah cell. To generalize this polynomial law to other cells, the value of C-rate needs to be re-evaluated for different cell capacities. It is assumed that the impact of nominal cell capacity C_{nom} is proportional to the value of the two capacitances. Therefore, the capacitance values are standardized by a proportional factor K calculated through Eq. (30).

$$K = \frac{C_{nom}}{13} \quad (30)$$

The Figure 15 shows the variation of resistances R_0, R_{pa} and R_{pc} as a function of SoC and C-rate. The charge transfer resistance R_{pa} is strongly dependent on the SoC, while the mass transfer resistance R_{pc} and the series resistance R_0 are less influenced by the SoC, which is consistent with the literature [26–28]. Indeed, the charge transfer impedance is much more strongly affected by the SoC than the series resistance and the mass transfer resistance. The current affects the mass transfer impedance but its impact is not significant, so it was not implemented in the model. R_0 and R_{pc} are then considered to be constant when the SoC of the cell varies. As for R_{pa}, the mean resistance value $\overline{R_{pa}}$ taken for the different C-rates was considered. The evolution of $\overline{R_{pa}}$ is shown in Figure 15d. The variation of $\overline{R_{pa}}$ tends to be stable when the SoC is larger than 0.5. Accordingly, the value of R_{pa} when the SoC is larger than 0.5 ($\overline{R_{pa}|_{SoC>0,5}}$) is averaged to 1.024 mΩ (Eq. (31)). A polynomial law of order 3 is then identified to express the variation of the ratio between $\overline{R_{pa}}$ and $\overline{R_{pa}|_{SoC>0,5}}$. This polynomial function is shown in Eq. (32).

$$\overline{R_{pa}|_{SoC>0.5}} = 1.024 \ m\Omega \quad (31)$$

$$\overline{R_{pa}} = \overline{R_{pa}|_{SoC>0.5}} \times (-15.00SoC^3 + 29.83SoC^2 - 18.98SoC + 4.85) \quad (32)$$

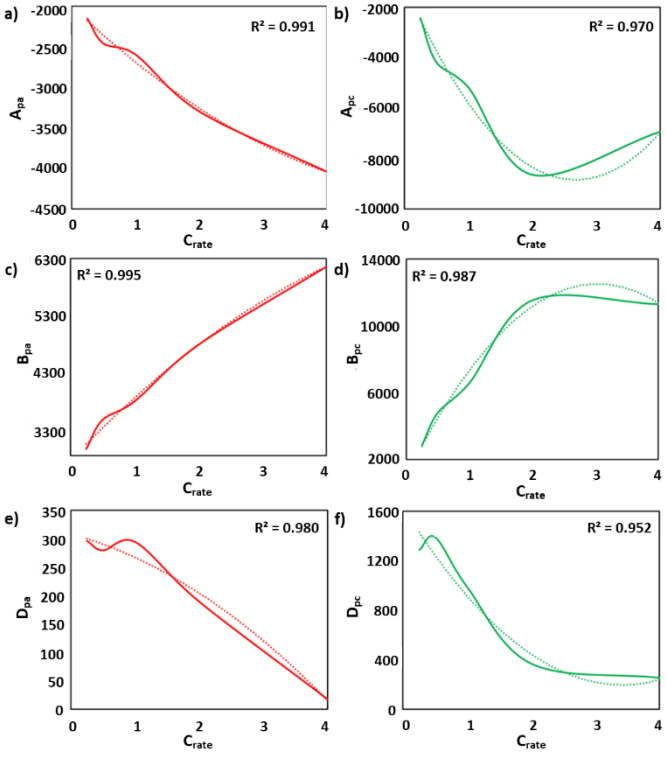

Fig. 13. Polynomial functions of C-rate to express the Apa (a), Bpa (c), Dpa (e), Apc (b), Bpc (d), Dpc (f) parameters of the capacitances Cpa and Cpc.

In Figure 16, the evolution of the R_0, R_{pa} and R_{pc} are shown for the different C-rates. For a SoC larger than 0.5, R_0, R_{pa} (i.e. $\overline{R_{pa}|_{SoC>0,5}}$) and R_{pc} represents around 50%, 35% and 15% of the sum of the 3 resistances respectively. The following distribution laws (Eq. (33), Eq. (34), Eq. (35), Eq. (36)) of the internal resistance are then determined:

$$R_0 = R_{int} \times 50\% \quad (33)$$

$$\overline{R_{pa}|_{SoC>0.5}} = R_{int} \times 35\% \quad (34)$$

$$\overline{R_{pa}} = R_{int} \times 35\% \times (-15.00SoC^3 + 29.83SoC^2 - 18.98SoC + 4.85) \quad (35)$$

$$R_{pc} = R_{int} \times 15\% \quad (36)$$

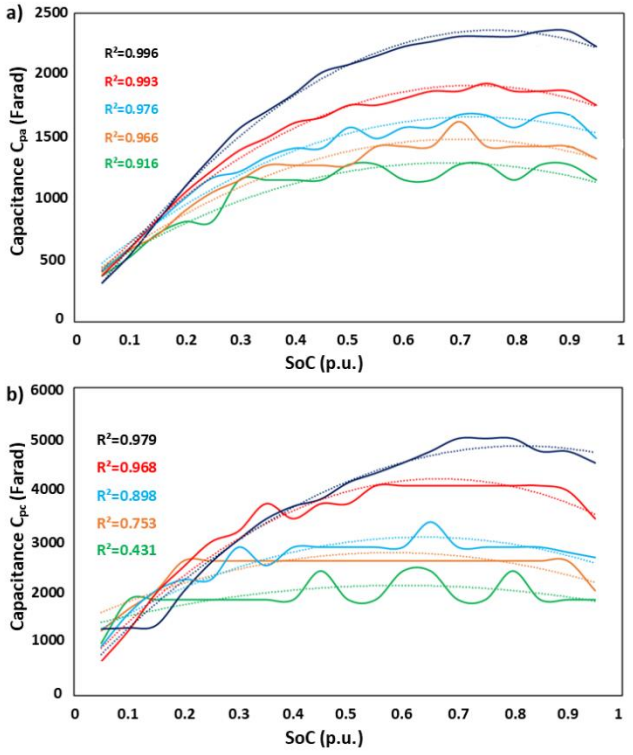

Fig. 14. a) Simulated (dashed curves) and experimental (solid curves) capacitance values of C_{pa} (a) and C_{pc} (b) under different SoC and C-rate levels (0.25C (green), 0.5C (orange), 1C (blue), 2C (red) and 4C (black)). The R^2 values shows the correlation between the experimental and the simulated data. The SoC is expressed in p.u. (100%=1 p.u.).

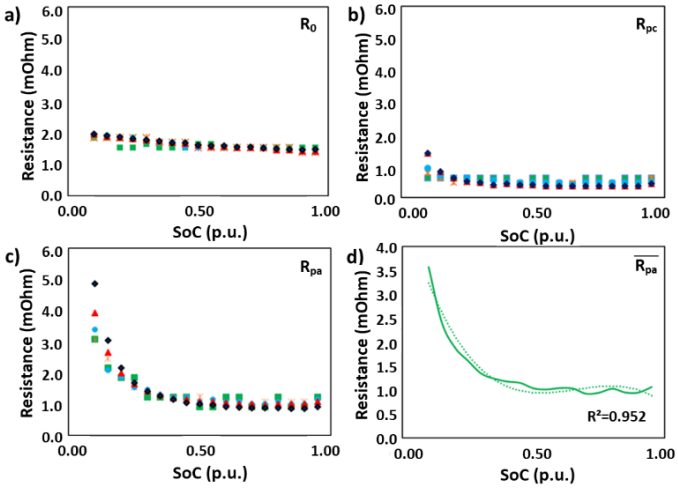

Fig. 15. Variation of resistance R0 (a), Rpc (b), Rpa (c) and $\overline{R_{pa}}$ (d) values depending on the SoC for a C-rate of 0.25C (green squares), 0.5C (orange stars), 1C (blue dots), 2C (red triangles), 4C (black diamonds). The SoC is expressed in p.u. (100%=1 p.u.).

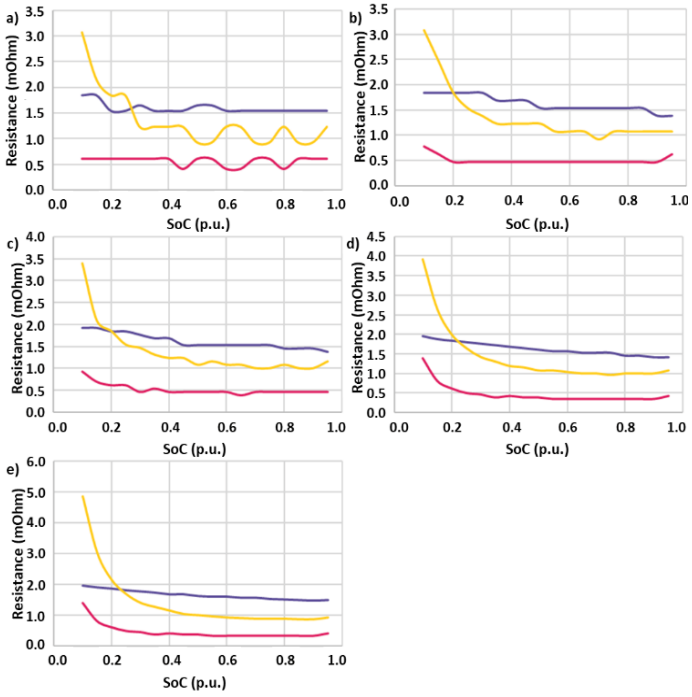

Fig. 16. Evolution of resistance R0 (blue), Rpa (yellow) and Rpc (red) as a function of SoC at a C-rate of 0.25C (a), 0.5C (b), 1C (c), 2C (d) and 4C (e). The SoC is expressed in p.u. (100%=1 p.u.).

When all parameters are defined and implemented in the model, realistic cell behavior curves are obtained. The simulation of a 10 A discharge of a 25 Ah capacity cell at 15°C is shown in Figure 17. As expected, the model simulates correctly the voltage decrease and a well-defined relaxation period is obtained afterwards.

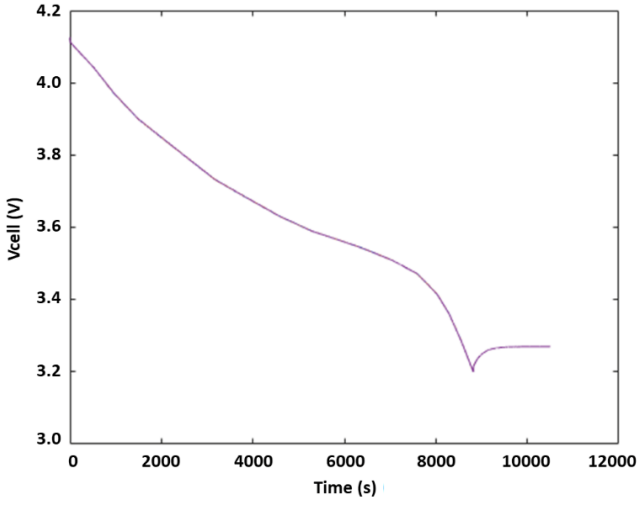

Fig. 17. Simulation of a 25 Ah cell discharge at 10 A at T=15°C.

3.2 Failure-mode results

In order to test the sturdiness of this model, a more realistic current profile, a Worldwide harmonized Light vehicles Test Cycle

(WLTC) was applied. The 30 minutes speed vs time WLTC cycle was converted into a current vs time profile, using the fundamental principle of dynamics and a simplified electric motor model. The cycle is then repeatedly applied on a loop, until one of the battery cells reaches a SoC of 10%. The cells were then recharged at 2C rate until a cell reaches a SoC of 95%, at which point the WLTC cycles resumed. A 2p2s battery was tested in series/parallel and parallel/series configurations. The simulation starts with all the cells at 10% SoC, setting off the charge procedure. The cell n°1 is set to be disconnected from the circuit after 10000s. Figure 18 shows the result obtained with a series/parallel configuration (Figure 18a). When the cell n°1 is disconnected, its current becomes equal to zero and cell n°2 compensates with a current which is twice as much as the original value (Figure 18b). This results in a deterioration of cell n°2 that charges up to a higher SoC (Figure 18c). Fewer WLTC cycles are performed, and a larger amount of heat is produced by cell n°2 (Figure 18d). As expected, the sub-circuit made of cells n°3 and n°4 remains unchanged.

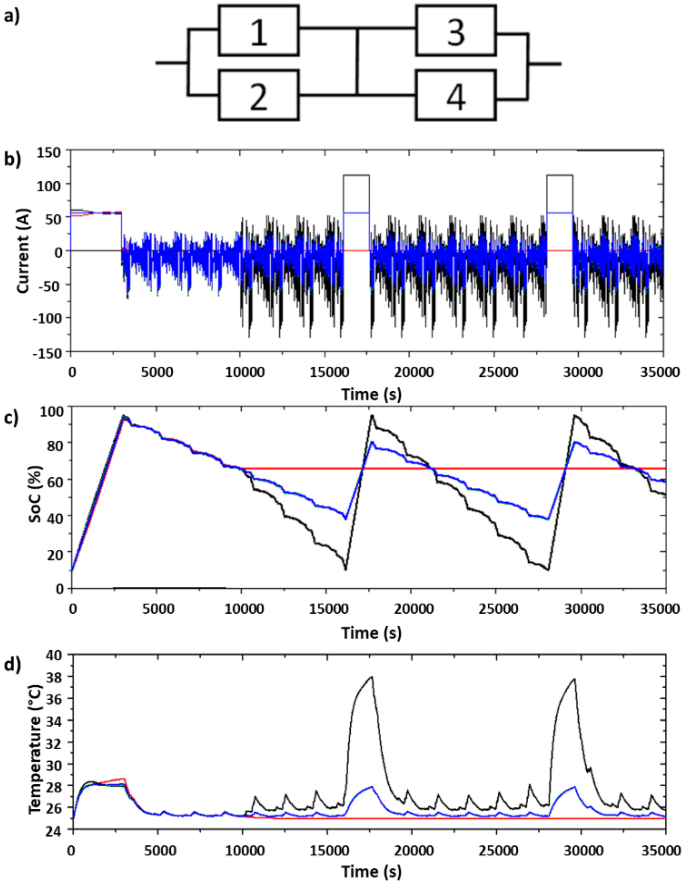

Fig. 18. Simulation results for a 2p2s battery with disconnection of a cell in a series/parallel configuration (a). Evolution of the current (b), SoC (c) and temperature (d) as a function of time for the cell n°1 (red), cell n°2 (black), cell n°3 (green) and cell n°4 (blue).

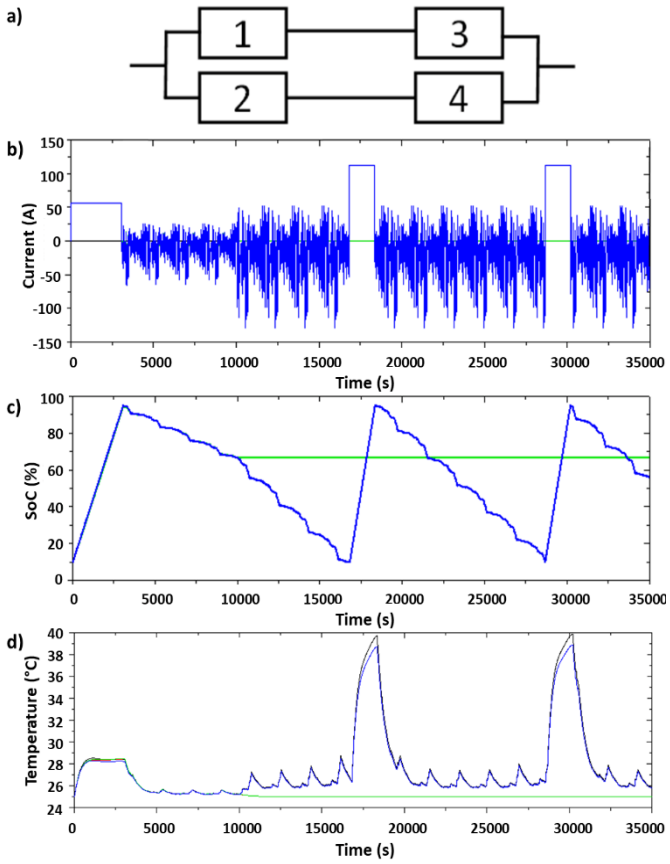

Fig. 19. Simulation results for a 2p2s battery with disconnection of a cell in a parallel/series configuration (a). Evolution of the current (b), SoC (c) and temperature (d) as a function of time for the cell n°1 (red), cell n°2 (black), cell n°3 (green) and cell n°4 (blue).

The model also works when using parallel/series configuration, the result of the simulation is shown in Figure 19. The disconnection of the cell n°1 results in the by-pass of cells n°1 and n°3, making all the current flow through the cells n°2 and n°4 (Figure 19b) and making those cells reach the SoC limits faster (Figure 19c). This increase of current flow increases the amount of heat released, as shown by the significant increase of temperature of these two cells up to 38-39°C (Figure 19d).

3.3 Ageing results

3.3.1 Calendar ageing

To verify the relevance of our calendar ageing model, the simulated data given by the model were compared with experimental data obtained from calendar ageing tests carried out on NMC and LFP batteries [10,24].

First, the calendar ageing of a NMC battery was studied. The same battery characteristics were used as the one studied in the reference [24] : a 43 Ah NMC battery. Capacity loss data were generated for different temperatures (0°C, 25°C, 45° and 60°C) at a given SoC of 80% and those data were compared to the experimental data presented in reference [24]. The comparison between

the experimental results and the simulated results is shown in Figure 20. It is shown that for temperatures close to the ambient one (45°C and 25°C), good correlation is obtained between the simulated data and the experimental data. However, for higher or lower temperatures (0°C and 60°C), there is a significant gap between the 2 sets of data. This can be explained by the fact that our model was calibrated on a rather small temperature range. Among the hypotheses taken for the calibration, it was assumed that, for a given SoC level on a fixed duration, the evolution of performance degradation (capacity loss and resistance increase) is linear with temperature. When the temperature range is widened, this hypothesis becomes less accurate with a more significant error. However, the model and the tests give the same evolution for the performance degradation at the 4 different temperatures. The model can then be corrected by using a correction factor for the temperatures out of the calibration range (0°C and 60°C) determined with the experimental data of Keil et al. [23]. The corrected curves (dashed lines) for these two temperatures are shown in Figure 20. A correction factor of 2 was applied in that case.

Similarly, our simulation results were compared with the experimental data obtained from the tests performed by Redondo et al. [10]. They studied the performance degradation of 2.3 Ah LFP cells due to calendar ageing. The studies were carried out at 30°C for different SoCs (30%, 65% and 100%). Using the same cell characteristics, capacity loss data were generated with our model and compared to the experimental data presented in that work. The comparison between the experimental results and the simulated results is shown in Figure 21.

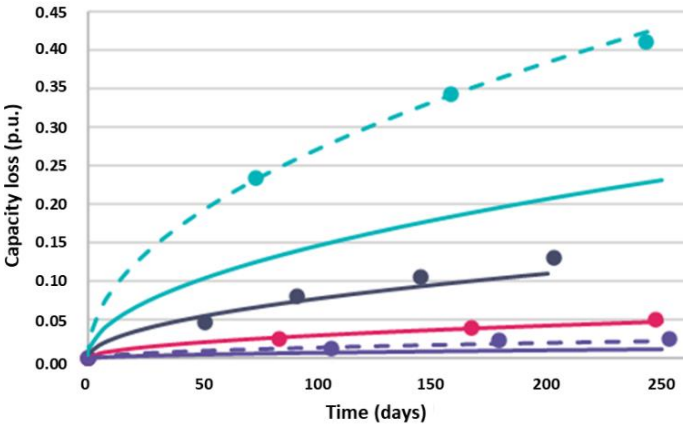

Fig. 20. Capacity loss as a function of time due to calendar ageing of a NMC cell at a SoC of 80% and at a temperature of 0°C (purple), 25°C (red), 45°C (black) and 60°C (green). Data obtained by experimental tests (dots) and simulations with (dashed lines) or without (solid lines) a corrective factor. The capacity loss is expressed in p.u. (100%=1 p.u.).

Good correlation is obtained between the simulated and the experimental data. The model and the tests give the same evolution for the performance degradation. However, a small gap between the experimental and the simulated data is observed. As previously, a corrective factor can be applied in the model to adjust this small error and get a better fit of the experimental data with the simulation. A corrective factor of 1.33 was applied in that case. The corrected curves are shown in Figure 21b.

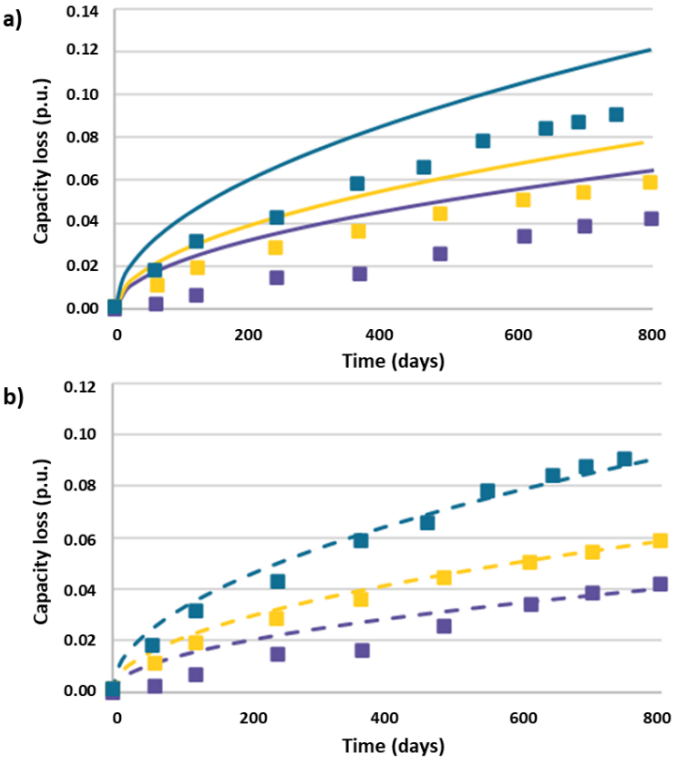

Fig. 21. Capacity loss as a function of time due to calendar ageing of a LFP cell at a SoC of 30% (purple), 65% (yellow), 100% (green) at 30°C. Data obtained by experimental tests (dots) and simulated data (lines). Simulated data obtained without (a, solid lines) and with (b, dashed lines) applying a corrective factor. The capacity losses are expressed in p.u. (100%=1 p.u.).

As a conclusion, our calendar ageing model can give a good estimation of a cell degradation when no current is applied. The simulation results are in good correlation with experimental data when the simulation temperature is maintained around an ambient temperature. If the temperature is out of the ideal temperature range around the ambient temperature (5-45°C), the model can be corrected with a correction factor. These defects are known pitfalls resulting from the use of an empirical strategy for the design of the model.

3.3.2 Cycle ageing

After being calibrated thanks to the data of Gao et al. [13], the model was compared to experimental data obtained at different temperatures published by Jalkanen et al. [12]. In their work, they investigated the performance degradation of 40 Ah NMC cells at a given cycling rate of 1C at different temperatures (25°C, 45°C and 65°C). Simulations were made with our model using the same cell characteristics. The comparison between the experimental and the simulated data is shown in Figure 22. At 25°C, similar evolutions of the capacity loss and resistance increase are obtained with the simulations compared to the experimental data. A rather good

correlation is obtained between the experimental and the simulated data at this temperature. However, a significant gap is observed between the experimental and the simulated values after a large number of cycles, both for the capacity loss and the resistance increase. The model is then adjusted by modifying the A_c and A_r values, to 7648 and 4203 respectively. The corrected simulated values show a much better correlation with the experimental data, regardless of the number of cycles. At 45°C, similar evolutions are observed for the experimental and the simulated data but with a more important gap between the values at large number of cycles. The model is then adjusted by modifying the A_c and A_r values, to 2264 and 4452 respectively. At 65°C, a similar evolution is observed for the experimental and the simulated data with an even more important gap between the values at large number of cycles for the capacity loss. For the resistance increase, a slightly better correlation is observed between the experimental and the simulated data for less than 1000 cycles.

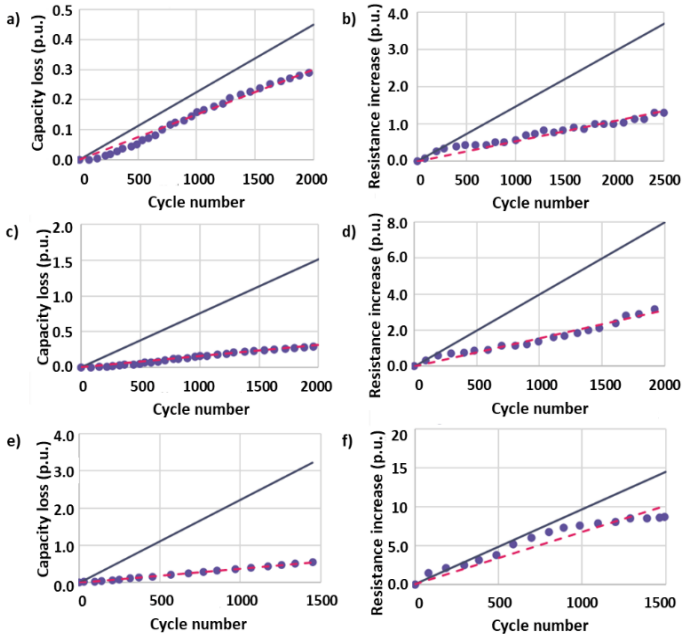

Fig. 22. Capacity loss (a, c, e) and resistance increase (b, d, f) of NMC cells after cycling at 1C at 25°C (a, b), 45°C (c, d) and 65°C (e, f). Simulated data, before (solid lines) and after applying a correction factor (dashed lines), compared to experimental data (dots) obtained from the study of Jalkanen et al. [12] The capacity losses and resistance increases are expressed in p.u. (100%=1 p.u.).

After 1000 cycles, the resistance increase is less important experimentally than the one obtained by simulation. In that case, the model is adjusted by modifying the A_c and A_r values, to 1922 and 8044 respectively.

Globally, the model gives larger values of capacity loss and resistance increase than the experimental data regardless of the temperature. In order to model properly the behavior of large capacity Li-ion battery cells that can be found in the automotive industry, it was chosen to adjust the model according to the experimental results presented in the work of Jalkanen et al. [12], as they have been studying cells with larger capacities than those of Gao et al. [13], previously used to calibrate the model. As shown previously, this modification was necessary to obtain simulation results showing good correlation with the experimental data of Jalkanen et al. [12].

4. Conclusion

In this paper, an overall simulation analysis and an evaluation of a new and accurate lithium-ion battery model is provided. This model comprises a simulation of the battery cell relaxation period with ageing predictions and a cell-failure/disconnection mode. Using the Kirchhoff laws and the Dual Polarisation equivalent circuit model (R + RC + RC circuit), the overall behavior of the battery pack is obtained from those of the individual cells. This type of model gives a strong dynamic response to the voltage and gives a good approximation of the chemical behavior of a real battery. The relaxation process was also modelled thanks to the equivalent circuit model. This phase is often neglected in empirical modellings, which often causes an error in the state of charge estimation for the BMS for instance, thus affecting its accuracy. For the battery pack ageing model, the degradation can be modelled on a long-time scale and with exposure to a fast sampling of values (in the order of seconds), contrary to many current models that need much longer calculation times to predict the battery ageing. The ageing model comprises a calendar ageing model and a cycle ageing model, both calibrated thanks to experimental data. Simulations are then carried out and compared to other experimental data to verify the reliability of the model. The model gives good results, with good correlation with experimental data when the simulation temperature is maintained around an ambient temperature. However, when the simulation temperature is too far from the ambient temperature (lower than 5°C or larger than 45°C), the model must be corrected by setting up correction factors. Modellings of cell failures were also implemented. Unlike the modellings available in the accessible literature, the failure mode presented here is not a predictive model (to predict when the failure will happen) but it offers a direct response for the regulation of the battery in case of a cell disconnection (random or programmed). To improve the model further, more literature work will be carried out so that various technologies (LFP, NMC, NCA) can be better distinguished within the battery pack's model results. An experimental approach will also be carried out to validate these proposed models.

Acknowledgment

This work was carried out at Altran Prototypes Automobiles (APA) as a part of the Hybrid Innovative Powertrain (HIP) project within the Capgemini Engineering Research and Innovation Department. The authors would like to thank Jia YU and Zenjabil JOUINI for their contribution to the work.

Conflict of Interest Statement

The authors declare there is no conflict of interest in this study.

CRediT Author Statement

Adrien Soloy: Writing-original draft, writing-review & editing, supervision, validation,
Thomas Bartoli: Writing-original draft, data curation, formal analysis,
Fatima Haidar: Writing-review & editing

References

[1] O'Connell A, Pavlenko N, Bieker G, Searle S. A comparison of the life-cycle greenhouse gas emissions of european heavy-duty vehicles and fuels. 2023 févr. (The International Council on Clean Transportation).

[2] Regulation (EU) 2019/631 of the European Parliament and of the council of 17 April 2019 setting CO2 emission performance standards for new passenger cars and for new light commercial vehicles, and repealing Regulations (EC) No 443/2009 and (EU) No 510/2011. 2019. (Official Journal of the European Union).

[3] Liu K, Li K, Peng Q, Zhang C. A brief review on key technologies in the battery management system of electric vehicles. Front Mech Eng. 2019;14(1):47-64.

[4] Singh KV, Bansal HO, Singh D. A comprehensive review on hybrid electric vehicles: architectures and components. J Mod Transport. 2019;27(2):77-107.

[5] Hu X, Xu L, Lin X, Pecht M. Battery Lifetime Prognostics. Joule. 2020;4(2):310-46.

[6] Ouyang T, Xu P, Chen J, Lu J, Chen N. Improved parameters identification and state of charge estimation for lithium-ion battery with real-time optimal forgetting factor. Electrochim Acta. 2020;353:136576.

[7] Fellner C, Newman J. High-power batteries for use in hybrid vehicles. J Power Sources. 2000;85(2):229-36.

[8] Miao Y, Hynan P, von Jouanne A, Yokochi A. Current Li-Ion Battery Technologies in Electric Vehicles and Opportunities for Advancements. Energies. 2019;12(6):1074.

[9] Zeng X, Li M, Abd El-Hady D, Alshitari W, Al-Bogami AS, Lu J, et al. Commercialization of Lithium Battery Technologies for Electric Vehicles. Adv Energy Mater. juill 2019;9(27):1900161.

[10] Redondo-Iglesias E, Venet P, Pelissier S. Modélisation du vieillissement calendaire de cellules lithium-ion (graphite/LiFePO4) avec prise en compte de la dérive de leur état de charge. In: Symposium de Génie Electrique (SGE'16). Grenoble, France; 2016.

[11] Badey Q. Étude des mécanismes et modélisation du vieillissement des batteries lithium-ion dans le cadre d'un usage automobile. [Paris XI]: Université Paris-Sud; 2012.

[12] Jalkanen K, Karppinen J, Skogström L, Laurila T, Nisula M, Vuorilehto K. Cycle aging of commercial NMC/graphite pouch cells at different temperatures. Appl Energy. sept 2015;154:160-72.

[13] Gao Y, Jiang J, Zhang C, Zhang W, Ma Z, Jiang Y. Lithium-ion battery aging mechanisms and life model under different charging stresses. J Power Sources. 2017;356:103-14.

[14] Eom SW, Kim MK, Kim IJ, Moon SI, Sun YK, Kim HS. Life prediction and reliability assessment of lithium secondary batteries. J Power Sources. 2007;174(2):954-8.

[15] Ganjeizadeh F, Tapananon T, Lei H. Predicting Reliability of Lithium Ion Batteries. International Journal of Engineering Research and Technology. 2014;3(8):1189-92.

[16] Lee S, Kim J, Lee J, Cho BH. State-of-charge and capacity estimation of lithium-ion battery using a new open-circuit voltage versus state-of-charge. J Power Sources. 2008;185(2):1367-73.

[17] He H, Xiong R, Fan J. Evaluation of Lithium-Ion Battery Equivalent Circuit Models for State of Charge Estimation by an Experimental Approach. Energies. 2011;4(4):582-98.

[18] Madani S, Schaltz E, Knudsen Kær S. An Electrical Equivalent Circuit Model of a Lithium Titanate Oxide Battery. Batteries. 2019;5(1):31.

[19] Li A. Analyse expérimentale et modélisation d'éléments de batterie et de leurs assemblages : application aux véhicules électriques et hybrides [Energie électrique]. Université Claude Bernard - Lyon I; 2013.

[20] Łebkowski A. Temperature, Overcharge and Short-Circuit Studies of Batteries used in Electric Vehicles. Prz Elektrotech. 2017;1(5):69-75.

[21] Amine K, Liu J, Belharouak I. High-temperature storage and cycling of C-LiFePO4/graphite Li-ion cells. Electrochem Commun. 2005;7(7):669-73.

[22] Lin X, Perez HE, Mohan S, Siegel JB, Stefanopoulou AG, Ding Y, et al. A lumped-parameter electro-thermal model for cylindrical batteries. J Power Sources. juill 2014;257:1-11.

[23] Keil P, Schuster SF, Wilhelm J, Travi J, Hauser A, Karl RC, et al. Calendar Aging of Lithium-Ion Batteries: I. Impact of the Graphite Anode on Capacity Fade. J Electrochem Soc. 2016;163(9):A1872-80.

[24] Ben-Marzouk M, Chaumond A, Redondo-Iglesias E, Montaru M, Pélissier S. Experimental Protocols and First Results of Calendar and/or Cycling Aging Study of Lithium-Ion Batteries – the MOBICUS Project. WEVJ. 24 juin 2016;8(2):388-97.

[25] Yuksel T, Michalek J. Development of a Simulation Model to Analyze the Effect of Thermal Management on Battery Life. In 2012. p. 2012-01-0671.

[26] Redondo Iglesias E. Étude du vieillissement des batteries lithium-ion dans les applications « "véhicule électrique" »: combinaison des effets de vieillissement calendaire et de cyclage. Université de Lyon 1; 2017.

[27] Zarrin H, Farhad S, Hamdullahpur F, Chabot V, Yu A, Fowler M, et al. Effects of Diffusive Charge Transfer and Salt Concentration Gradient in Electrolyte on Li-ion Battery Energy and Power Densities. Electrochimica Acta. avr 2014;125:117-23.

[28] Karthikeyan DK, Sikha G, White RE. Thermodynamic model development for lithium intercalation electrodes. Journal of Power Sources. déc 2008;185(2):1398-407.